Journal of Advanced Ceramics
2022, **11**(5): 702–711
https://doi.org/10.1007/s40145-021-0560-4
ISSN 2226-4108
CN 10-1154/TQ

Research Article

Rare earth monosilicates as oxidation resistant interphase for SiC_f/SiC CMC: Investigation of SiC_f/Yb_2SiO_5 model composites

Xirui LV[a,b], Mengkun YUE[c,d], Xue FENG[c,d], Xiaoyan LI[c,d], Yumin WANG[e], Jiemin WANG[a], Jie ZHANG[a,*], Jingyang WANG[a,*]

[a]*Shenyang National Laboratory for Materials Science, Institute of Metal Research, Chinese Academy of Sciences, Shenyang 110016, China*
[b]*School of Materials Science and Engineering, University of Science and Technology of China, Shenyang 110016, China*
[c]*AML, Department of Engineering Mechanics, Tsinghua University, Beijing 100084, China*
[d]*Center for Mechanics and Materials, Tsinghua University, Beijing 100084, China*
[e]*Institute of Metal Research, Chinese Academy of Sciences, Shenyang 110016, China*

Received: August 3, 2021; Revised: November 3, 2021; Accepted: December 3, 2021

Abstract: Model composites consisting of SiC fiber and Yb_2SiO_5 were processed by the spark plasma sintering (SPS) method. The mechanical compatibility and chemical stability between Yb_2SiO_5 and SiC fiber were studied to evaluate the potential application of Yb monosilicate as the interphase of silicon carbide fiber reinforced silicon carbide ceramic matrix composite (SiC_f/SiC CMC). Two kinds of interfaces, namely mechanical and chemical bonding interfaces, were achieved by adjusting sintering temperature. SiC_f/Yb_2SiO_5 interfaces prepared at 1450 and 1500 ℃ exhibit high interface strength and debond energy, which do not satisfy the crack deflection criteria based on He–Hutchison diagram. Raman spectrum analyzation indicates that the thermal expansion mismatch between Yb_2SiO_5 and SiC contributes to high compressive thermal stress at interface, and leads to high interfacial parameters. Amorphous layer at interface in model composite sintered at 1550 ℃ is related to the diffusion promoted by high temperature and DC electric filed during SPS. It is inspired that the interfacial parameters could be adjusted by introducing $Yb_2Si_2O_7$–Yb_2SiO_5 interphase with controlled composition to optimize the mechanical fuse mechanism in SiC_f/SiC CMC.

Keywords: silicon carbide fiber reinforced silicon carbide ceramic matrix composite (SiC_f/SiC CMC); interphase; rare earth (RE) silicates; interfacial parameters

1 Introduction

Silicon carbide fiber reinforced silicon carbide ceramic matrix composites (SiC_f/SiC CMCs) are considered as promising materials for high temperature applications, including the core of gas turbine engines [1,2]. It is well accepted that the mechanical behavior of SiC_f/SiC CMCs depends not only on the intrinsic properties of fiber and matrix, but also on the properly-designed fiber–matrix bonding [3,4]. Actually, the fiber–matrix bonding is controlled by the interphase deposited on

* Corresponding authors.
E-mail: J. Zhang, jiezhang@imr.ac.cn;
J. Wang, jywang@imr.ac.cn

fiber surface prior to the deposition of matrix. Interphase provides fiber–matrix bonding which is weak enough to deflect matrix cracks and strong enough to transfer load between fiber and matrix. Moreover, interphase should protect fiber against aggressive species during preparation and application. Boron nitride (BN) and pyrolytic carbon (PyC) have been proven to provide appropriate fiber–matrix bonding to achieve non-brittle fracture behavior of SiC_f/SiC CMCs. However, gas turbine engines are generally operating in a tough environment featured by high temperature oxidation humid atmosphere, which will lead to severe degradation of BN and PyC interphase [5]. The degradation process of SiC_f/SiC CMCs with BN [6,7] and PyC [8] interphase in oxidation humid environment has been detailedly reported in the scale of mini-composite [9] and two-dimensional (2D) fiber tow reinforced composites. The main drawback of PyC interphase is its low oxidation resistance, and BN is limited by its intrinsic water vapor sensitivity.

Several methods have been proposed to minimize the degradation of interphase, including (1) providing additional protection through environmental barrier coatings (EBCs) [10,11], self-healing matrix [12,13], and protective SiC layers; (2) doping current interphase materials with self-healing elements to enhance oxidation resistance [14]. Both approaches have limitation on the extent to which they improve oxidation resistance. Another solution is to replace PyC or BN with functionally equivalent and oxidation-resistant new interphase materials [5]. Rare earth (RE) silicates are considered to be promising candidates [15,16]. In our previous work [17], $Yb_2Si_2O_7$ was considered as an effective interphase in SiC_f/SiC CMC and weak interface was maintained after sintering at 1250 ℃. Fiber push-out tests of $SiC_f/Yb_2Si_2O_7$ model composites showed weak interface with debond energy of 0.4–1.8 J/m^2, which satisfied the crack deflection criteria of energy release rate. Sliding stress of weak $SiC_f/Yb_2Si_2O_7$ interface was 7.6–17.5 MPa, which was comparable to weak PyC- or BN-fiber interface. No reaction zone was observed in model composite sintered at 1450 ℃, which proved excellent chemical stability between $Yb_2Si_2O_7$ and SiC. Moreover, it has been reported that $Y_2Si_2O_7$ and $Ho_2Si_2O_7$ were prepared on the surface of SiC fiber through a dip coating method, suggesting that it is possible to coat SiC fiber with RE disilicates [15].

State-of-the-art SiC_f/SiC CMCs serving in turbine engines usually have the interphase prepared by chemical vapor infiltration (CVI) methods, and compared with PyC and BN, it is difficult to prepare stoichiometric multicomponent oxides by CVI. Ito *et al*. [18,19] prepared Y–Si–O films through laser chemical vapor deposition and Y_2SiO_5 appeared as minor phase in $Y_2Si_2O_7$ film. In the binary phase diagram of RE_2O_3–SiO_2, $RE_2Si_2O_7$ is presented as straight line [20], and thus the synthesis of single phase $RE_2Si_2O_7$ compounds needs very strict control of the RE/Si ratio, and RE_2SiO_5 often appears as a secondary phase in the preparation of $RE_2Si_2O_7$. On the one hand, some intrinsic properties of RE monosilicates differ significantly from RE disilicates. For $Yb_2Si_2O_7$ interphase, the participation of Yb_2SiO_5 may bring influence on the mechanical fuse mechanism in SiC_f/SiC CMCs. In addition, few researches were conducted to illuminate the feasibility of applying Yb_2SiO_5 as interphase in SiC_f/SiC CMCs as most of work was focused on its application on EBCs. RE monosilicates do not show phase transformation from room temperature to melting point and exert better resistance to water vapor and CMAS corrosion compared with corresponding RE disilicates [11,21]. Moreover, the elastic moduli of RE monosilicates are lower than those of corresponding disilicates, which are beneficial for crack deflection according to Cook and Gorden mechanism [22]. Therefore, it is inspired that RE monosilicates are also potential interphase candidates and it is necessary to clarify their influence to promote the application of RE disilicate interphase.

In order to illustrate the potential effects of RE monosilicates and demonstrate the feasibility of applying RE monosilicate interphase in SiC_f/SiC CMCs, we herein processed model composites consisting of SiC fiber and Yb_2SiO_5 sintered by spark plasma sintering (SPS). Yb_2SiO_5 is selected to compare with the corresponding disilicates in our previous work [17]. The interfacial sliding stress and debond energy during fiber push-out were reported, and the mechanical compatibility and chemical stability between SiC and Yb_2SiO_5 were investigated.

2 Materials and method

2.1 Synthesis and characterization of SiC_f/Yb_2SiO_5 interfaces

Model composites in our work consisted of chemical vapor deposited (CVD) SiC fibers and Yb_2SiO_5 powder, and the synthesis of model composites was detailedly

reported in Ref. [17]. Long SiC fibers with an average diameter of ~100 μm were manufactured by chemical vapor deposition of β-SiC onto a ~10 μm diameter W core, and the ratio of Si:C is 1.06:1. The cross section and surface of SiC fiber are shown in Fig. 1. Pure phase Yb_2SiO_5 powder was prepared by pressureless sintering, and the particle size was ~1 μm. The X-ray diffraction (XRD) patterns obtained through D8 Advance (Bruker, Germany) and the scanning electron microscopy (SEM) image of Yb_2SiO_5 powder are shown in Fig. 2. Sintering temperatures were selected as 1450, 1500, and 1550 ℃, and the obtained model composites were labeled as YbMS-1450, YbMS-1500, and YbMS-1550, respectively. Densities of model composites were measured by Archimedes' method. Cross section of interfaces in model composites were assessed by the SUPRA 35 scanning electron microscope (LEO, Oberkochen, Germany). Microstructures of SiC_f/Yb_2SiO_5 interface in model composites were assessed by the transmission electron microscope (FEI Themis Titan G2 cubed 60–300, the Netherlands). The transmission electron microscopy (TEM) samples were prepared by the focused ion beam (FIB, FEI Helios Nanolab 600i, the Netherlands).

2. 2 Measurement of interfacial parameters

Fiber push-out test was performed through a nano-mechanical test instrument equipped with a Berkovich indenter (TI 950 Tri-boIndenter, Hysitron, USA) to obtain the load–displacement curves. The front and back sides of samples after push-out test were observed by SEM. 3–5 curves were obtained successfully for each model composite. Interfacial parameters of model composites were obtained by analyzing the load–displacement curves of single fiber push-out test, which was detailedly reported in Ref. [17]. The maximum load to initiate interface debonding (P_d) and the steady-state load during sliding (P_f) were determined. The interfacial parameters were calculated by

$$\Gamma_{RE} = (1-2\nu_f k)P_d^2/(4\pi^2 r^3 E_f) \quad (1)$$

$$k = E_m\nu_f/[E_f(1+\nu_m)+E_m(1-\nu_f)] \quad (2)$$

$$\tau = P/(2\pi rt) \quad (3)$$

where Γ_{RE} is the interfacial debonding energy of SiC_f/Yb_2SiO_5 interface; r, ν_f, and E_f are the fiber radius, Poisson's ratio, and modulus, respectively; ν_m and E_m are the matrix Poisson's ratio and modulus, respectively; k is an elastic factor related to fiber and matrix elastic properties; t is the sample thickness in the push-out test. The interfacial strength and sliding stress were calculated by corresponding load (P) normalized by $2\pi rt$.

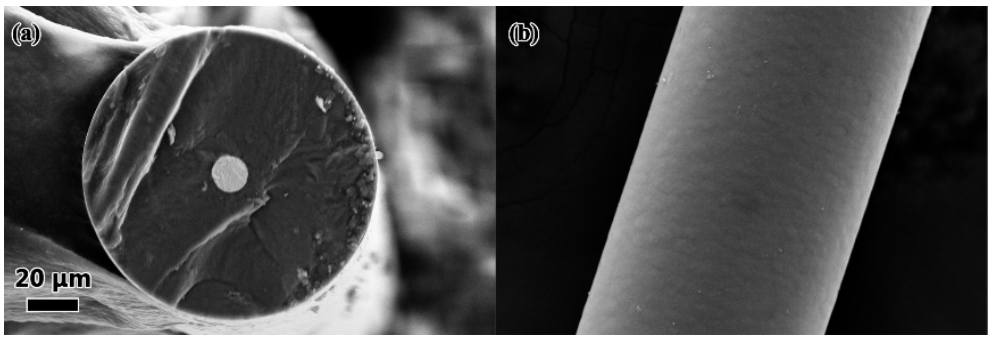

Fig. 1 SEM images of (a) cross section and (b) surface of CVD SiC fiber.

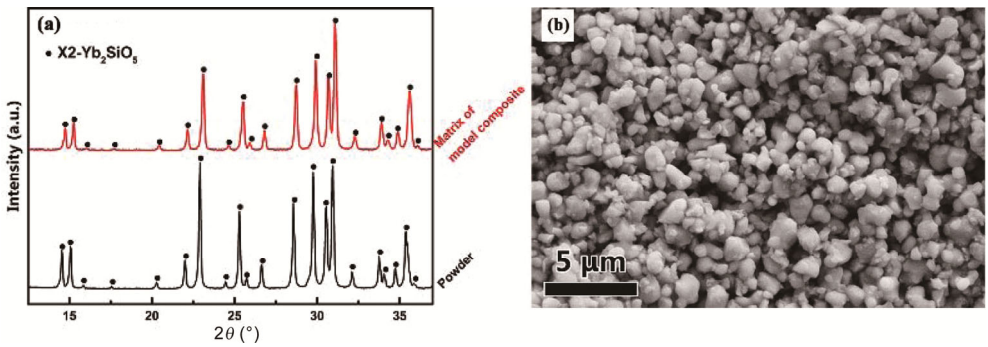

Fig. 2 (a) XRD patterns and (b) SEM image of Yb_2SiO_5.

2. 3 Mechanical compatibility investigation between SiC fiber and Yb_2SiO_5

Micro-Raman spectroscopy focused on SiC adjacent to SiC_f/Yb_2SiO_5 interface was utilized to investigate local thermal residual stress at interface in model composites. The position of Raman peaks will shift as residual stress is appeared, and the shifts in Raman band can be used to obtain the stress with very high spatial resolution [23−25]. It has been reported that pure bulk β-SiC exhibits two sharp bands arising from two optical phonon modes (transverse optical phonon mode (TO) peak at ~790 cm^{-1} and the longitudinal optical phonon mode (LO) peak at ~973 cm^{-1}) [26]. The displacement value of TO peak and the residual stress satisfy the following linear relationship:

$$\Delta\omega_{TO}(cm^{-1}) = -3.27\sigma(GPa) \quad (4)$$

where $\Delta\omega_{TO} = \omega_{TO} - \omega_{0TO}$, ω_{0TO} is the TO peak value in a freestanding SiC fiber, ω_{TO} is the TO peak value of SiC fiber embedded in the model composites, and σ is the residual stress of SiC fiber. Raman spectroscopy was performed using a LabRAM HR800 (HORIBA, France). The excitation light was He–Ne laser with emitting radiation at 632.82 nm, and laser beam spot size was 2 μm. The scan range of all Raman spectra was 600–1200 cm^{-1}. The test points were selected 5–10 μm away from the interface. Peak separation was processed by software Peakfit, and the wavenumber positions corresponding to respective peaks were determined. Moreover, the residual stress in radial direction (σ_r) at interface can be approximated using the following classical equation [27]:

$$\sigma_r = -E_m(\alpha_m - \alpha_f)\Delta T / (1 + \nu_m) \quad (5)$$

where the misfit stress generated is a function of the difference (ΔT) between processing and ambient temperature, elastic modulus (E_m) and Poisson's ratio of matrix (ν_m), and the coefficient of thermal expansion mismatch between the matrix (α_m) and fiber (α_f).

2. 4 Chemical compatibility investigation between SiC and Yb_2SiO_5

The intrinsic chemical compatibility between SiC and Yb_2SiO_5 was investigated by thermal analysis of powder mixtures. Pure phase Yb_2SiO_5 powder and commercial SiC powder (Shanghai Chaowei Nano-technology Co., Ltd., Shanghai, China) were mixed and ground at a molar ratio of 1:1. The analysis was conducted using the thermogravimetry–differential scanning calorimetry (TG–DSC) (STA 449 F3 Jupiter, NETZSCH, Germany). The sample was heated to 1600 ℃ at a rate of 10 ℃/min in Ar. The mixture of Yb_2SiO_5 and SiC (molar ratio of 1:1) was also isothermally treated in Ar at 1500 ℃ for 1 h in an Al_2O_3 tube furnace, and the XRD results before and after heat treatment were analyzed.

3 Results

3. 1 Characterization of sintered model composites

The morphologies of polished cross section of model composites are shown in Fig. 3. The white part in the center of SiC fiber is tungsten core which served as a carrier of CVD silicon carbide. Well-adhered SiC fiber/Yb_2SiO_5 interfaces are observed in three model composites, and the Yb_2SiO_5 matrix in YbMS-1450 (Fig. 3(a)) shows lower density than that of the other two model composites. The experimental densities of YbMS-1450, YbMS-1500, and YbMS-1550 are 6.30, 6.93, and 7.14 g/cm^3, respectively.

3. 2 Interfacial parameters

3.2.1 Fiber push-out test

During fiber push-out test, the upper surface of SiC fiber was pushed by the Berkovich indenter, and then the load was transferred to fiber/Yb_2SiO_5 interface by

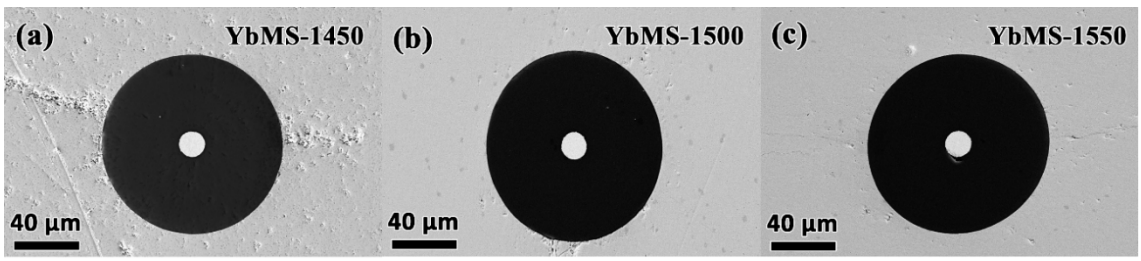

Fig. 3 Cross sections of interfaces in (a) YbMS-1450, (b) YbMS-1500, and (c) YbMS-1550 perpendicular to the SiC fiber.

intact fiber. Fiber push-out was observed in YbMS-1450 and YbMS-1500, but not in YbMS-1550. As load increased, the SiC fiber surface cracked before interface debonded due to stress concentration at the tip of indenter, and the cracked fiber could not be pushed-out. Typical load–displacement curves of fiber push-out tests are shown in Fig. 4(a). Interface debonds completely at maximum load and the load drops suddenly due to rapid movement of the fiber and indenter after debonding. Figure 4(d) displays the back side of samples after push-out test. The push-out length is ~10 μm and no noticeable damage or deformation is identified on the protruding fiber. The load–displacement curve of no pushed-out YbMS-1550 sample is shown in Fig. 4(b). The maximum value of applied load has reached the limit of our equipment. The front side of no pushed-out YbMS-1550 sample is shown in Fig. 4(e). The indentation and tip cracks demonstrate that fiber surface was broken before the interface debonded. Therefore, it is deduced that the interfacial parameters of YbMS-1550 are higher than those of YbMS-1450 and YbMS-1500. In a typical push-out test, the indenter pushes fiber to move downward after interface debonds completely, leading to dynamic sliding. The sliding is often reflected by a "near-plateau" part following the maximum value in the load–displacement curve, which was observed in our previous work [17], and the steady-state load is used to calculate the interfacial sliding stress. In the present work, the indenter knocked Yb_2SiO_5 matrix due to rapid movement after the interface debonded so that the steady sliding could not be obtained. Therefore, push-back test was performed to obtain interfacial sliding stress on the debonded interface. Specimens after fiber push-out test were turned over and the fiber was pushed again to obtain the sliding stress at debonded interface. As shown in Fig. 4(c), characteristic load–displacement curve of fiber push-back exhibits similar progress with fiber push-out test. The back side of sample after fiber push-back test is shown in Fig. 4(f). The sinking fiber is pushed back from the reverse direction. Through comparing Fig. 4(a) with 4(c), it is perceived that the applied load to induce movement of SiC fiber is lower during the push-back. During push-out, the applied load overcame interface bonding originating from interlock of surface irregular asperities inherent at interface and friction stress induced by thermal stress [28]. In push-back test, the applied load only overcame the friction stress as the interlock was broken in push-out. Therefore, it is reasonable to calculate the sliding stress according to the push-back load [29]. Table 1 summarizes the interfacial strength, sliding stress, and debond energy of model composites in this work, and the characteristic interfacial parameters of weak $SiC_f/Yb_2Si_2O_7$ from our previous work [17] are listed for comparison.

3.2.2 *Interfacial residual stress*

Figure 5 shows Raman spectra of freestanding SiC fiber, SiC fiber in YbMS-1450, SiC fiber in YbMS-1500, and SiC fiber in YbMS-1550. The $SiC_f/Yb_2Si_2O_7$ model composite sintered at 1250 ℃ (labeled as YbDS-

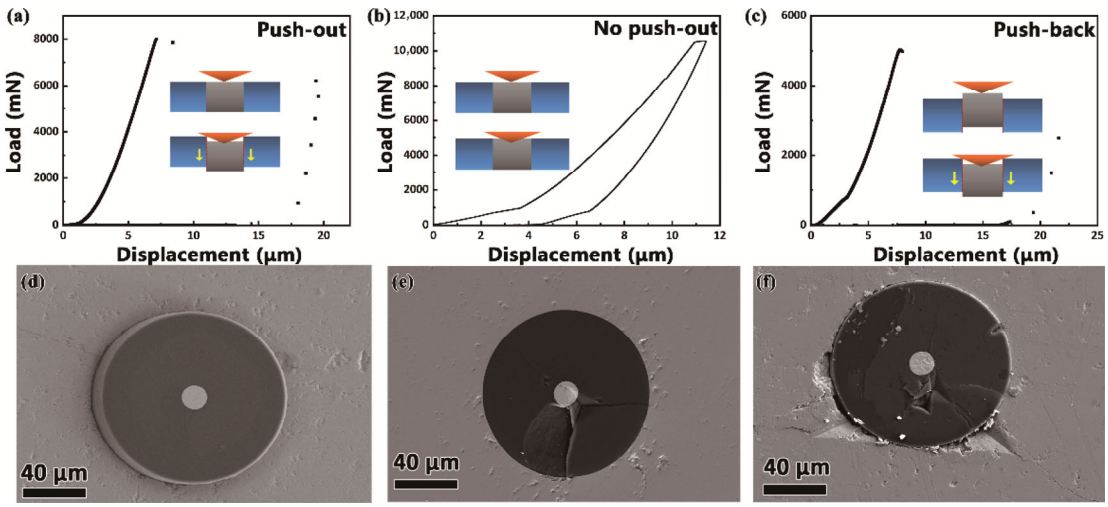

Fig. 4 Load–displacement curves and SEM images of fiber push-out test. (a) The typical curve of YbMS-1450 and YbMS-1500 in which the fiber was pushed out and (d) the back side of pushed-out sample. (b) The curve of YbMS-1550 sample in which the fiber was not pushed out and (e) the cross section of cracked fiber. (c) The characteristic curve of the push-back and (f) the back side of pushed-back sample.

Table 1 Interfacial parameters, including interfacial strength (τ_d), sliding stress (τ_f), debond energy (Γ_{RE}), ratio of interfacial debond energy to fiber fracture energy (Γ_i/Γ_f), and the thermal residual stress obtained by Raman spectra (σ) and calculated by Eq. (5) of the model composites

Model composite	τ_d (MPa)	τ_f (MPa)	Γ_{RE} (J/m^2)	Γ_i/Γ_f	σ (GPa)	σ_r (GPa)
YbDS-1250 [17]	18.8±0.9	17.5±2.7	1.8±0.2	0.09	0.57±0.2	0.32
YbMS-1450	53.1±6	—	17.3±5	0.87	0.88±0.2	0.79
YbMS-1500	61.7±18	34.6±14	27.1±12	1.36	0.95±0.2	0.82
YbMS-1550	—	—	—	—	1.06±0.1	0.80

Γ_i is the debonding energy of interface, which is equal to Γ_{RE} obtained by the push-out test, and Γ_f is the fracture energy of SiC fiber.

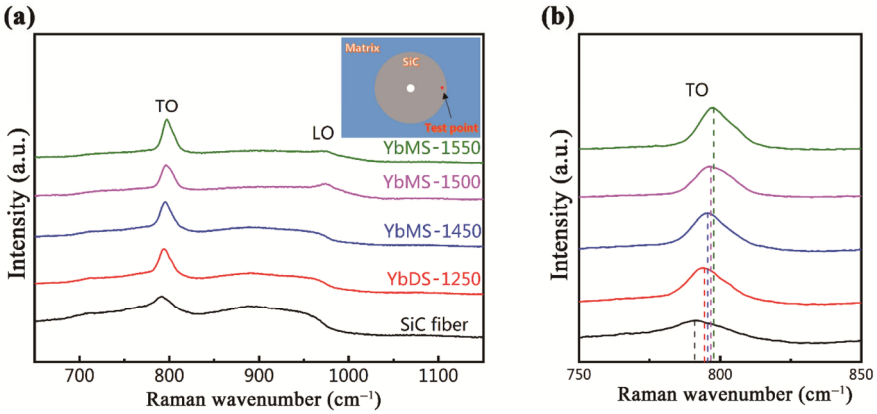

Fig. 5 (a) Characteristic Raman spectra of SiC obtained from different model composites near interface, and the inset shows the schematic diagram of test point on cross section of the SiC fiber. (b) The shifts of TO peaks in Raman spectra.

1250) was tested for comparison. The Raman spectra for different fibers exhibit similar features. As shown in Fig. 5(a), a sharp and intense TO peak is detected at ~790 cm^{-1}, and a broad LO peak at 800–960 cm^{-1} is observed in all of spectra. In addition, a shoulder band near by the TO peak appears at ~760 cm^{-1}, and the characteristic TO peak is asymmetrically broadened to the lower wavenumber. Moreover, a broad hump centered at ~880 cm^{-1} is located between TO and LO peaks. The features concluded above are related to various disorders in SiC crystals, including stacking faults, defects, grain boundaries, and amorphous phases [30]. Compared with LO peak, TO peak is less sensitive to defects in crystal structures, and the residual stress is calculated according to the shifts of TO peak. Compared with free SiC fiber, the TO peak of SiC fiber in model composites moves to high wavenumber, as shown in the local spectra around TO peak in Fig. 5(b), indicating that interfaces are under compressive stress in the model composites. Three to five patterns were obtained for each specimen, and the TO peaks of SiC in freestanding fiber YbD-S1250, YbMS-1450, YbMS-1500, and YbMS-1550 are 790.9, 792.7, 793.7, 794.0, and 794.3 cm^{-1}, respectively, as shown in Fig. 5(b). Table 1 summarizes the interfacial residual stresses (σ) at the interface of model composite which are calculated according to Eq. (5).

3.3 Chemical compatibility between SiC and Yb_2SiO_5

Figure 6(a) shows the TG–DSC curves obtained by heating a powder mixture of Yb_2SiO_5 and SiC in Ar. The baseline was subtracted before analysis. It is found that neither endothermic peak nor exothermal peak is observed in the DSC curve, and a sudden weight loss begins just above 1400 ℃, which is thought to reflect the gas generation. To reveal the potential reaction products between Yb_2SiO_5 and SiC, the mixed powder was isothermally treated at 1500 ℃ in an Al_2O_3 tube furnace under Ar atmosphere for 1 h. As shown in Fig. 6(b), the phase composition of treated powder is pretty much similar with that of raw powder.

The microstructure characterization of the as-sintered model composites is focused on the interface between SiC fiber and Yb_2SiO_5. Figure 7(a) displays a typical low magnification TEM image of interface in YbMS-1550, and SiC fiber adheres well with Yb_2SiO_5 matrix without noticeable cracks or pores. In the

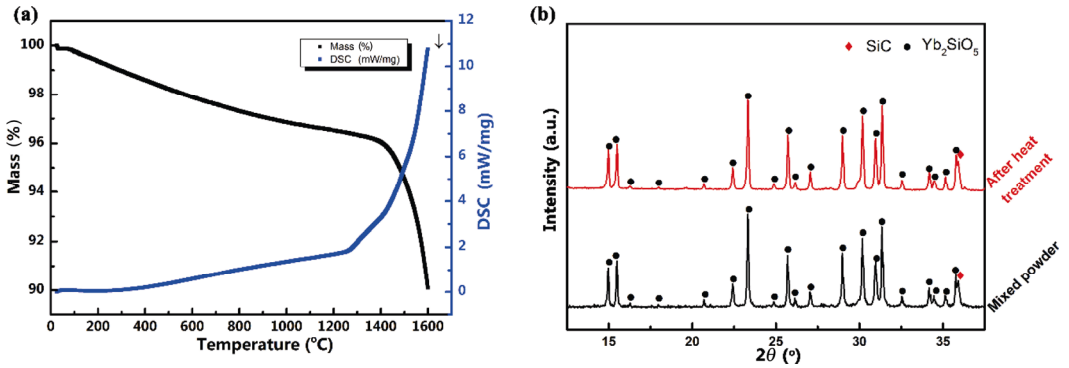

Fig. 6 (a) TG–DSC curves for the powder mixture of SiC and Yb_2SiO_5; (b) XRD patterns of mixed powder before and after the isothermal treatment.

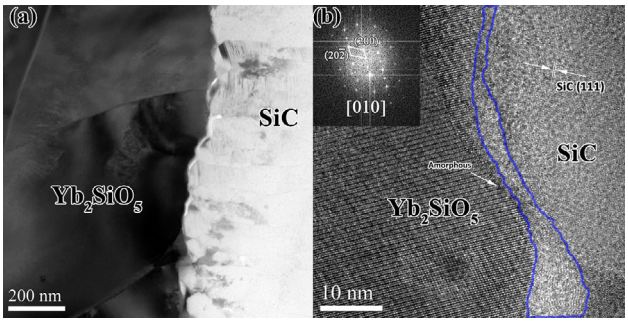

Fig. 7 (a) TEM image of a characteristic interface in YbMS-1550; (b) HRTEM of interface between SiC and Yb_2SiO_5. The fast Fourier transform image of Yb_2SiO_5 illustrates the orientation of Yb_2SiO_5, and the (111) lattice plane of SiC is marked by the arrow symbol. Amorphous layer is observed at the interface.

HRTEM morphology in Fig. 7(b), amorphous layer is observed and marked between Yb_2SiO_5 and SiC.

4 Discussion

4. 1 Feasibility of applying Yb_2SiO_5 interphase in SiC_f/SiC CMCs

According to the crack deflection criteria based on energy release rate, cracks will deflect at interface when [17]:

$$\Gamma_i / \Gamma_f < 0.4 \quad (6)$$

As summarized in Table 1, the Γ_i/Γ_f values of YbMS-1450 and YbMS-1500 are figured with the Γ_f value of 20 J/m^2 from Ref. [16]. The results of YbMS-1450 and YbMS-1500 are calculated to be 0.87 and 1.36, respectively, not satisfying the crack deflection criteria. Compared with weak $SiC_f/Yb_2Si_2O_7$ interface, SiC_f/Yb_2SiO_5 interface exerts a strong interface which could adhere tightly to the SiC fiber in SiC_f/SiC CMC.

4. 2 Formation of strong SiC_f/Yb_2SiO_5 interface and inspiration for SiC_f/SiC CMCs

The mechanical compatibility and chemical stability at SiC_f/Yb_2SiO_5 interface are investigated to elucidate the formation of strong interface. First of all, it has been reported that, compared with $Yb_2Si_2O_7$, Yb_2SiO_5 exhibits higher coefficient of thermal expansion (CTE) [31,32]. In model composite, the microstructure is assumed to be an assembly of uniformly sized, elastic, and spherical fiber surrounded by a semi-infinite matrix ($Yb_2Si_2O_7$ or Yb_2SiO_5). As model composite was cooled from processing temperature down to ambient temperature, a matrix with higher CTE should shrink more, placing the interface in residual compression. The values of thermal residual stress obtained by Raman spectrum vary from 0.88 to 1.06 GPa among three model composites, which are much higher than those of weak interface in YbDS-1250 (0.57 GPa). The residual stress was also calculated according to Eq. (5), and the results are summarized in Table 1. Compared with corresponding experimental results, the calculated values are slightly lower, and exhibit similar trend. Higher compressive stress in radial direction means that the fiber is gripped tightly by surrounding matrix, contributing to higher interfacial parameters in push-out test. According to the crack deflection criteria based on stress filed [22], higher compressive stress will also counteract the tensile stress at crack tip near interface, and block interface debonding.

The chemical stability at interface is another issue in the application of interphase. Firstly, neither endothermic peak nor exothermal peak is observed in the DSC curve, proving the chemical stability between Yb_2SiO_5 and SiC. Similar results have been observed in TG–DTA curves of powder mixture of Y_2SiO_5 and SiC,

which have been reported by Kato *et al*. [33]. Moreover, as similar mass loss phenomenon was observed in their work, they conducted mass analysis on the generated gases during TG–DTA of Y_2SiO_5 and SiC to reveal the origin of weight loss. The results indicated the generated gases composed of SiO and CO, both of which were typical reaction products of the active oxidation of SiC. It is deduced that the Ar atmosphere provided a low O_2 pressure [34,35] to induce this oxidation. According to Fig. 6(b), phase composition of powder after heat treatment is pretty much similar with that of raw powder, which also reveals the chemical stability between SiC and Yb_2SiO_5. In order to remove the influence of the SiC oxidation during experimental investigation, thermodynamic calculations carried out by Seifert *et al*. [36] confirmed the chemical stability between Y_2SiO_5 and SiC. Based on the experimental results and thermodynamic calculations, it is deduced that amorphous layer at SiC/Yb_2SiO_5 interface in YbMS-1550 is related to SPS processing. It has been reported that interface diffusion was promoted by local high temperature and DC electric filed during SPS [37], and the amorphous diffusion layer was maintained by the rapid cooling. Therefore, the interface in YbMS-1550 is difficult to form in actual CMC processing. According to the mechanical and chemical analysis, the mechanical bonding in YbMS-1450 and YbMS-1500 is enhanced by high compressive stress in radial direction arising from high CTE mismatch. The enhanced interface could grab fiber tightly, because debonding is inhibited by high interfacial parameters. Thereafter, cracks can be deflected at matrix/interphase interface or within interphase when the fiber/interphase interface is enhanced, and the environment does not have direct access to fiber, prohibiting the strong bonding between neighbored fibers resulted from rapid oxidation [38].

It is also inspired that Yb_2SiO_5 could be combined with $Yb_2Si_2O_7$ to tune the CTE of interphase in SiC_f/SiC CMC and adjust the interfacial parameters to accomplish the optimal mechanical fuse function. It has been reported that the $Yb_2Si_2O_7$–Yb_2SiO_5 composite environment coating possessed an intermediate CTE value between those of $Yb_2Si_2O_7$ and Yb_2SiO_5, and bulk samples of $Yb_2Si_2O_7$–Yb_2SiO_5 composites with different compositions exhibited tunable mechanical and thermal physical properties [39,40]. An estimation of debonding energy based on the rule of mixture was conducted to predict the crack deflection capacity of mixed interphase. Firstly, the interfacial strength and debonding energy satisfy Eq. (7) [17]:

$$\Gamma_{\mathrm{RE}} = [1 - 2\nu_{\mathrm{f}} k / (E_{\mathrm{f}} r)] L^2 \tau_{\mathrm{d}}^2 \tag{7}$$

where L is the typical sample thickness in fiber push-out test. Moreover, the interfacial strength of mixed interphase (τ_{dmix}) is calculated as Eq. (8):

$$\tau_{\mathrm{dmix}} = (1 - x)\tau_{\mathrm{dYbDS}} + x\tau_{\mathrm{dYbMS}} \tag{8}$$

where x is the content of Yb monosilicate, τ_{dYbDS} and τ_{dYbMS} are typical interfacial strengths of $Yb_2Si_2O_7$ and Yb_2SiO_5, respectively, in our work. As $\Gamma_{\mathrm{i}}/\Gamma_{\mathrm{f}} < 0.4$ is the criterion for crack deflection, the variation of $\Gamma_{\mathrm{i}}/\Gamma_{\mathrm{f}}$ value along with monosilicate content is exhibited in Fig. 8. As shown in Fig. 8, the debonding energy increases with monosilicate content, and the value of $\Gamma_{\mathrm{i}}/\Gamma_{\mathrm{f}}$ is close to 0.4 when x = 0.5. The diagram indicates that fiber/interphase bonding could be properly increased by controlling the content of Yb monosilicate in the Yb disilicate interphase, and the strengthened interface could maintain the mechanical fuse function and increase energy dissipation during fiber pull-out [41,42]. Moreover, the relationship between the interphase composition and interfacial parameters will be established, providing the guideline for the application of RE silicate interphase.

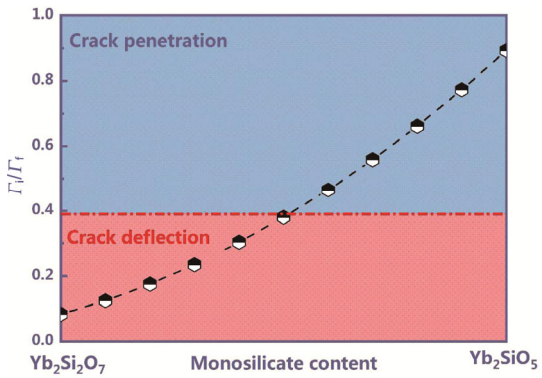

Fig. 8 Relation between $\Gamma_{\mathrm{i}}/\Gamma_{\mathrm{f}}$ value and the monosilicate content.

5 Conclusions

We herein report the characteristics of three SiC_f/Yb_2SiO_5 model composites with different interface characteristics to illustrate the potential influence of Yb_2SiO_5 to composite interphase. The interfaces in YbMS-1450 and YbMS-1500 exhibit high interfacial strength and debond energy, but do not fulfill the debond criteria derived from He–Hutchinson crack

deflection diagram. The sliding stresses of the samples are also higher than those of the typical weak interphase like PyC and BN. Raman spectrum shows that the CTE misfits between Yb_2SiO_5 and SiC contributed to strong interface bonding. Fiber in YbMS-1550 is not pushed out and amorphous layer is observed at the interface. The chemical stability between Yb_2SiO_5 and SiC is investigated through powder TG–DSC, and further analysis shows that the chemical bonding in model composite is due to the SPS processing. These results suggest that Yb_2SiO_5 could be applied to protect SiC fiber in CMCs, and also indicate that it is possible to adjust the interfacial parameters of $SiC_f/Yb_2Si_2O_7$ by controlling the content of Yb_2SiO_5 to optimize the mechanical fuse mechanism in SiC_f/SiC CMC.

Acknowledgements

This work was supported by the National Key R&D Program of China (No. 2017YFB0703201), the National Natural Science Foundation of China (No. 51772302), and CAS International Cooperation Key Program (No. 174321KYSB20180008).

References

[1] Steibel J. Ceramic matrix composites taking flight at GE Aviation. *Am Ceram Soc Bull* 2019, **98**: 30–33.

[2] Padture NP. Advanced structural ceramics in aerospace propulsion. *Nat Mater* 2016, **15**: 804–809.

[3] Naslain RR. The design of the fibre-matrix interfacial zone in ceramic matrix composites. *Compos A Appl Sci Manuf* 1998, **29**: 1145–1155.

[4] Kerans R, Parthasarathy T. Crack deflection in ceramic composites and fiber coating design criteria. *Compos A Appl Sci Manuf* 1999, **30**: 521–524.

[5] Kerans RJ, Hay RS, Parthasarathy TA, *et al*. Interface design for oxidation-resistant ceramic composites. *J Am Ceram Soc* 2002, **85**: 2599–2632.

[6] Carminati P, Jacques S, Rebillat F. Oxidation/corrosion of BN-based coatings as prospective interphases for SiC/SiC composites. *J Eur Ceram Soc* 2021, **41**: 3120–3131.

[7] Diaz OG, Marquardt K, Harris S, *et al*. Degradation mechanisms of SiC/BN/SiC after low temperature humidity exposure. *J Eur Ceram Soc* 2020, **40**: 3863–3874.

[8] Wang LY, Luo RY, Cui GY, *et al*. Oxidation resistance of SiC_f/SiC composites with a PyC/SiC multilayer interface at 500 ℃ to 1100 ℃. *Corros Sci* 2020, **167**: 108522.

[9] Lu ZL, Yue JL, Fu ZY, *et al*. Microstructure and mechanical performance of SiC_f/BN/SiC mini-composites oxidized at elevated temperature from ambient temperature to 1500 ℃ in air. *J Eur Ceram Soc* 2020, **40**: 2821–2827.

[10] Tejero-Martin D, Bennett C, Hussain T. A review on environmental barrier coatings: History, current state of the art and future developments. *J Eur Ceram Soc* 2021, **41**: 1747–1768.

[11] Tian ZL, Zhang J, Sun LC, *et al*. Robust hydrophobicity and evaporation inertness of rare-earth monosilicates in hot steam at very high temperature. *J Am Ceram Soc* 2019, **102**: 3076–3080.

[12] Luan XG, Zou Y, Hai XH, *et al*. Degradation mechanisms of a self-healing $SiC_{(f)}/BN_{(i)}/[SiC–B_4C]_{(m)}$ composite at high temperature under different oxidizing atmospheres. *J Eur Ceram Soc* 2018, **38**: 3804–3813.

[13] Tan X, Liu W, Cao LM, *et al*. Oxidation behavior of a 2D-SiC_f/BN/SiBCN composite at 1350–1650 ℃ in air. *Mater Corros* 2018, **69**: 1227–1236.

[14] Sathiyamoorthy R, Prakash KS, Sathishkumar C, *et al*. Investigation on SiC_f/SiC composites with SiBN interface processed through chemical vapor infiltration. *Mater Today Proc* 2016, **3**: 4220–4225.

[15] Boakye EE, Mogilevsky P, Hay RS, *et al*. Rare-earth disilicates as oxidation-resistant fiber coatings for silicon carbide ceramic–matrix composites. *J Am Ceram Soc* 2011, **94**: 1716–1724.

[16] Boakye EE, Mogilevsky P, Parthasarathy TA, *et al*. Processing and testing of $RE_2Si_2O_7$ fiber-matrix interphases for SiC–SiC composites. *J Am Ceram Soc* 2016, **99**: 415–423.

[17] Lv XR, Yue MK, Yang WF, *et al*. Tunable strength of SiC_f/β-$Yb_2Si_2O_7$ interface for different requirements in SiC_f/SiC CMC: Inspiration from model composite investigation. *J Mater Sci Technol* 2021, **67**: 165–173.

[18] Ito A, Endo J, Kimura T, *et al*. High-speed deposition of Y–Si–O films by laser chemical vapor deposition using Nd: YAG laser. *Surf Coat Technol* 2010, **204**: 3846–3850.

[19] Ito A, Endo J, Kimura T, *et al*. Eggshell- and fur-like microstructures of yttrium silicate film prepared by laser chemical vapor deposition. *Mater Chem Phys* 2011, **125**: 242–246.

[20] Costa GCC, Jacobson NS. Mass spectrometric measurements of the silica activity in the Yb_2O_3–SiO_2 system and implications to assess the degradation of silicate-based coatings in combustion environments. *J Eur Ceram Soc* 2015, **35**: 4259–4267.

[21] Tian ZL, Zhang J, Zhang TY, *et al*. Towards thermal barrier coating application for rare earth silicates RE_2SiO_5 (RE = La, Nd, Sm, Eu, and Gd). *J Eur Ceram Soc* 2019, **39**: 1463–1476.

[22] Pompidou S, Lamon J. Analysis of crack deviation in ceramic matrix composites and multilayers based on the Cook and Gordon mechanism. *Compos Sci Technol* 2007, **67**: 2052–2060.

[23] Das B, Brodard P, Bandyopadhyay PP. Raman spectroscopy assisted residual stress measurement of plasma sprayed and laser remelted zirconia splats and coatings. *Surf Coat Technol* 2019, **378**: 124920.

[24] Jin XC, Sun YL, Hou C, *et al*. Investigation into cooling-rate dependent residual stresses in ZrB_2–SiC composites using improved Raman spectroscopy method. *Ceram Int* 2019, **45**: 22564–22570.

[25] Kollins K, Przybyla C, Amer MS. Residual stress measurements in melt infiltrated SiC/SiC ceramic matrix composites using Raman spectroscopy. *J Eur Ceram Soc* 2018, **38**: 2784–2791.

[26] Nakashima S, Harima H. Raman investigation of SiC polytypes. *Phys Stat Sol* (*a*) 1997, **162**: 39–64.

[27] Li LB. *Interfaces of Ceramic Matrix Composites: Design, Characterization and Damage Effects*. Weinheim, Germany: Wiley-VCH GmbH, 2020.

[28] Chandra N, Ghonem H. Interfacial mechanics of push-out tests: Theory and experiments. *Compos A Appl Sci Manuf* 2001, **32**: 575–584.

[29] Zhang LF, Ren CZ, Zhou CL, *et al*. Single fiber push-out characterization of interfacial mechanical properties in unidirectional CVI-C/SiC composites by the nano-indentation technique. *Appl Surf Sci* 2015, **357**: 1427–1433.

[30] Ward Y, Young RJ, Shatwell RA. Application of Raman microscopy to the analysis of silicon carbide monofilaments. *J Mater Sci* 2004, **39**: 6781–6790.

[31] Tian ZL, Zheng LY, Wang JM, *et al*. Theoretical and experimental determination of the major thermo-mechanical properties of RE_2SiO_5 (RE = Tb, Dy, Ho, Er, Tm, Yb, Lu, and Y) for environmental and thermal barrier coating applications. *J Eur Ceram Soc* 2016, **36**: 189–202.

[32] Zhou YC, Zhao C, Wang F, *et al*. Theoretical prediction and experimental investigation on the thermal and mechanical properties of bulk β-$Yb_2Si_2O_7$. *J Am Ceram Soc* 2013, **96**: 3891–3900.

[33] Kato M, Fukasawa T, Goto Y. Reactions in Y_2SiO_5–SiC and $Y_3Al_5O_{12}$–SiC in yttrium-silicate/silicon carbide layered composites. *J Ceram Soc Jpn* 2000, **108**: 861–864.

[34] Vaughn WL, Maahs HG. Active-to-passive transition in the oxidation of silicon carbide and silicon nitride in air. *J Am Ceram Soc* 1990, **73**: 1540–1543.

[35] Jacobson N, Harder B, Myers D. Oxidation transitions for SiC part I. Active-to-passive transitions. *J Am Ceram Soc* 2013, **96**: 838–844.

[36] Seifert HJ, Wagner S, Fabrichnaya O, *et al*. Yttrium silicate coatings on chemical vapor deposition-SiC-precoated C/C–SiC: Thermodynamic assessment and high-temperature investigation. *J Am Ceram Soc* 2005, **88**: 424–430.

[37] Munir ZA, Quach DV, Ohyanagi M. Electric field and current effects on sintering. *Sintering* 2012, **35**: 137–158.

[38] Morscher GN, Yun HM, DiCarlo JA, *et al*. Effect of a boron nitride interphase that debonds between the interphase and the matrix in SiC/SiC composites. *J Am Ceram Soc* 2004, **87**: 104–112.

[39] Wang X, Xue ZL, Zhou ZM, *et al*. Influence of $Yb_2Si_2O_7$ doping concentration on mechanical properties and thermal conductivity of Yb_2SiO_5–$Yb_2Si_2O_7$ composite ceramics. *J Alloys Compd* 2021, **889**: 161718.

[40] Garcia E, Sotelo-Mazon O, Poblano-Salas CA, *et al*. Characterization of $Yb_2Si_2O_7$–Yb_2SiO_5 composite environmental barrier coatings resultant from *in situ* plasma spray processing. *Ceram Int* 2020, **46**: 21328–21335.

[41] Rebillat F, Lamon J, Guette A. The concept of a strong interface applied to SiC/SiC composites with a BN interphase. *Acta Mater* 2000, **48**: 4609–4618.

[42] Rebillat F, Lamon J, Naslain R, *et al*. Properties of multilayered interphases in SiC/SiC chemical-vapor-infiltrated composites with “weak” and “strong” interfaces. *J Am Ceram Soc* 1998, **81**: 2315–2326.